Carbon Fluxes during Dansgaard–Oeschger Events as Simulated by an Earth System Model

Markus Jochum,[a] Zanna Chase,[b] Roman Nuterman,[a] Joel Pedro,[b] Sune Rasmussen,[a] Guido Vettoretti,[a] and Peisong Zheng[c]

[a] *Niels Bohr Institute, Copenhagen, Denmark*
[b] *University of Tasmania, Hobart, Australia*
[c] *Shantou University, Shantou, China*

ABSTRACT: The Community Earth System Model with marine and terrestrial biogeochemistry is configured to simulate glacial climate. The integration shows transitions from warm to cold states—interstadials to stadials—and back. The amplitude of the associated Greenland and Antarctica temperature changes and the atmospheric CO_2 signal are consistent with ice-core reconstructions, and so are the time lags between termination of a stadial, Antarctic temperature reversal, and the decline of the atmospheric CO_2 concentration (for brevity's sake simply referred to as CO_2 from here on). The present model results stand out because the transitions occur spontaneously (without forcing changes like hosing) and because they reproduce the observed features above in a configuration that uses the same parameterizations as climate simulations for the present day (i.e., no retuning has been done). During stadials, precipitation shifts lead to reduced growth on land, which dominates the CO_2 increase; the ocean acts as a minor carbon sink during the stadials. After the end of the stadials, however, the sudden reversal of the stadial anomalies in temperature, wind, and precipitation turns the ocean into a carbon source, which accounts for the continued rise of CO_2 for several hundred years into the interstadial. The simulations also provide a novel possible interpretation for the observed correlation between CO_2 and Antarctic temperature: rather than both being controlled by Southern Ocean processes, they are both controlled by the North Atlantic Ocean, and most of the extra CO_2 may not be of Southern Hemisphere origin. If the stadials are prolonged through North Atlantic hosing, the upper ocean comes to an equilibrium, and the CO_2 response is dominated by a single process: reduced export production in the North Atlantic as result of the collapsed overturning circulation. This is in contrast to the unforced simulation where the net ocean carbon flux anomaly is the sum of several regional responses of both signs and similar magnitudes. Reducing the aeolian iron deposition by half, to account for the observed reduction of Southern Hemisphere dust fluxes during stadials, reduces biological productivity and export production so that the Southern Ocean emerges as an important carbon source, at least for the three centuries up until a new equilibrium for the upper ocean is reached.

SIGNIFICANCE STATEMENT: The last ice age featured millennial-scale oscillations in CO_2 and temperature, the latter being anticorrelated between Greenland and Antarctica. This is often referred to as the bipolar seesaw. Here, an Earth system model is described that reproduces these signals, and its results are used to explain the observed correlation between temperature and CO_2. In contrast to previous idealized studies it is found that all ocean basins and the land each contribute equally to the CO_2 signal.

1. Introduction

During the last glacial, Greenland temperatures exhibited abrupt changes between warm interstadial and cold stadial conditions. We will refer to the sudden warmings as Dansgaard–Oeschger (D-O) events (Dansgaard et al. 1993). Numerical experiments suggest that they are initiated by sudden sea ice loss in the Nordic, Irminger, and Labrador Seas (Li et al. 2010; Peltier and Vettoretti 2014; Kleppin et al. 2015), which may be preceded by slow changes to ice sheets or CO_2 [Zhang et al. (2014) and Zhang et al. (2017), respectively]. There is observational evidence that they are associated with large changes of the Atlantic meridional overturning circulation (AMOC; Henry et al. 2016) and global monsoon systems (e.g., Corrick et al. 2020). During stadials, Antarctica warms, and then cools again during

the interstadials (Buizert et al. 2015a; Fig. 1), as does the South Atlantic (Barker et al. 2009; Anderson et al. 2021). The peaks in Antarctic warming, termed Antarctic Isotope Maximum (AIM) events, are accompanied by anomalies in CO_2 that range between several ppm for centennial-scale events to up to 20 ppm for millennial-scale events (Bauska et al. 2021). It is the goal of the present study to quantify in an Earth system model (ESM) the various processes that contribute to this stadial rise in CO_2.

The close relationship between anomalies in Antarctic temperature and CO_2 (Fig. 1) suggests a Southern Ocean control of the CO_2 increase (Ahn and Brook 2008), which is qualitatively supported by several chemical and biological proxies in Southern Ocean sediment records (R. F. Anderson et al. 2009; Gottschalk et al. 2016; Jaccard et al. 2016; Rae et al. 2018). Moreover, the model study of Menviel et al. (2015) suggests the stadial increase in Antarctic Bottom Water formation as a mechanism for increasing CO_2.
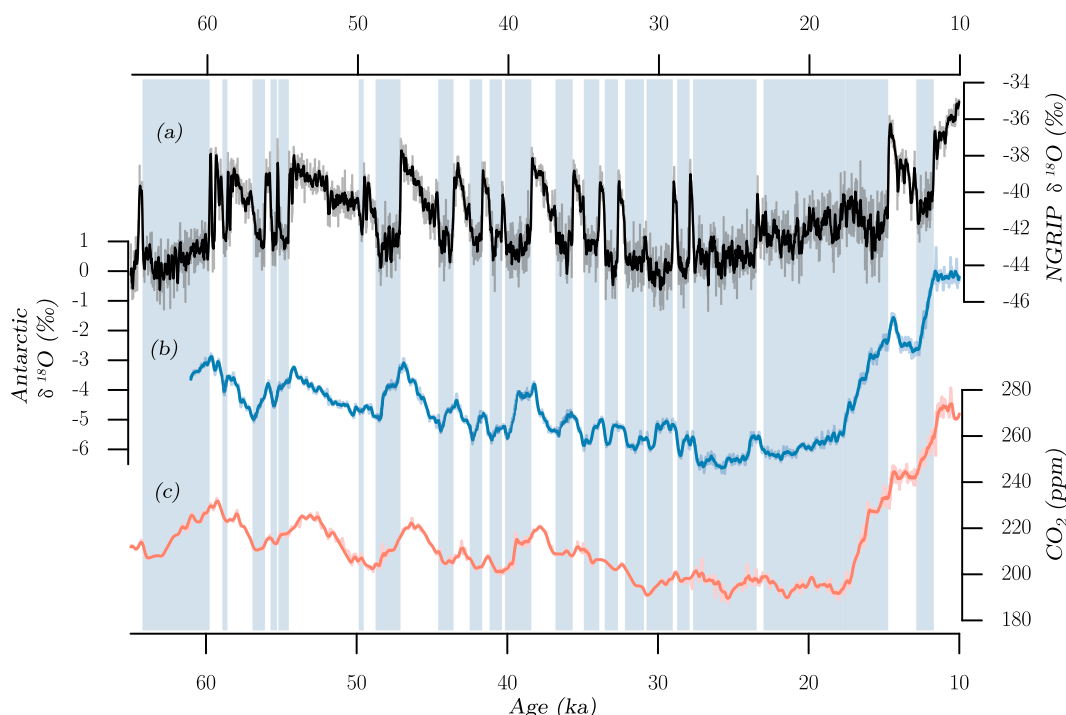
Corresponding author: Markus Jochum, mjochum@nbi.dk

FIG. 1. Millennial-scale climate events for the period from 65 to 10 kya. (a) The North Greenland Ice Core Project (NGRIP) ice-core oxygen-isotope (δ^{18}O) data as a temperature proxy (NGRIP members 2004). (b) Antarctic five-core averaged δ^{18}O record (Buizert et al. 2018). (c) Atmospheric CO_2 concentration measured in the West Antarctic Ice Sheet Divide ice core (Bauska et al. 2021). All records are on the WD2014 time scale (Buizert et al. 2015b). The light blue vertical shading shows the time spans of the Greenland stadials.

Another potentially important basin to contribute to the CO_2 fluctuations is the North Atlantic. Motivated by the weak stadial AMOC, several numerical studies have analyzed the response of the carbon cycle to AMOC collapse induced by freshwater forcing in the North Atlantic. They find an increase in CO_2 associated with an AMOC collapse. This is explained by a reduction in the efficiency of the biological pump, because the production of North Atlantic Deep Water (NADW), which is low in preformed nutrients, is decreased (e.g., Schmittner and Galbraith 2008). Land carbon, too, may contribute to the stadial CO_2 signal (Bauska et al. 2018), and terrestrial models find in response to stadial changes in temperature and precipitation a loss of terrestrial carbon in either the boreal regions (Scholze et al. 2003) or the tropics (Bozbiyik et al. 2011; Nielsen et al. 2019). All the studies above employ simplified model setups, either by decoupling the carbon cycle from the climate models or by using models of intermediate complexity. A thorough review of 55 of these simplified-model studies is provided by Gottschalk et al. (2019). They find that carbon flux responses to various forcing changes (e.g., air–sea flux changes in response to increased freshwater forcing) vary substantially from model to model; moreover, the net CO_2 responses are the results of several positive and negative feedbacks (e.g., loss of land carbon is compensated by increased oceanic uptake). Unfortunately, most of these results are plausible and we are faced with a conundrum: if our models cannot credibly reproduce the past, have we understood and accounted for the important processes?

The present study is an attempt to approach the issue from a different angle: rather than building a simple model with what we think we know, we use a full ESM, whose model–data mismatches can point us to things we do not know. Surprisingly, the Community Earth System Model (CESM1) can reproduce several important features of D-O events without changing its physical or biogeochemical parameterizations (with the exception of two; see next section) from their preindustrial configurations. However, large assumptions have to be made about the sizes of the Last Glacial Maximum (LGM) carbon pools, which are detailed in the next section. Section 3 describes the results of the numerical experiments, section 4 puts them into the context of observations and other model studies, and a summary in section 5 concludes our study.

2. Experimental design

We use the coarse-resolution version of CESM1 (Hurrell et al. 2013; Shields et al. 2012). It consists of models of the ocean, the atmosphere, sea ice, and land; they are connected through a coupler, which passes and interpolates fluxes between the various models. The ocean resolution varies smoothly with location, with resolutions of approximately 20 km around Greenland, 100 km in the Southern Ocean, and 400 km in the subtropical North Pacific. There are 60 vertical layers with nonuniform thickness, ranging from 10 m at the surface to 250 m at the bottom. The ocean model is run with the Gent and McWilliams (1990)

representation for mesoscale mixing and uses a stratification-dependent thickness and isopycnal diffusivity (Ferreira et al. 2005). The atmospheric model uses a T31 spectral truncation in the horizontal (3.75° resolution) with 26 vertical layers. In all the present simulations, changing CO_2 will change radiative forcing. Biogeochemistry is coupled to the climate system and actively exchanges carbon between ocean, atmosphere, and land. The ocean component includes diatoms, small phytoplankton, and diazotrophs, with phytoplankton growth controlled by temperature, light, and available nutrients (nitrate, phosphate, silicate, and iron; Moore et al. 2013; Lindsay et al. 2014). CESM1 has a fixed lysocline (i.e., the depth at which calcium carbonate remineralizes is fixed). Thus, the present setup does not allow for carbonate compensation, a feedback between ocean acidity and calcium carbonate sedimentation that is speculated to affect CO_2 on time scales of millennia or longer (e.g., Archer et al. 2000; Brovkin et al. 2007). The land component prognostically computes leaf and stem area indices and vegetation height using a prescribed spatial distribution of plant functional types (Lawrence et al. 2011).

The present-day coarse-resolution climate of CESM1 is in many aspects similar (i.e., it has the same biases) to its 10 times more expensive 1° resolution version (Shields et al. 2012); using 160 cores yields a simulation rate of 90 per day. In its present LGM configuration the stadials are not forced by freshwater hosing, but emerge spontaneously just as in its high-resolution version, and Vettoretti and Peltier (2018) describe in detail the physical aspects of the D-O events. Pedro et al. (2018) use a coarse-resolution LGM configuration of CCSM3, a predecessor of CESM1, the main difference of which is an improved representation of tropical convection (Neale et al. 2008). They show with hosing experiments how a collapse of the AMOC leads to Antarctic warming. The patterns, magnitude, and timing of the global response of the physical system in the present study is similar to the ones in Pedro et al. (2018) and Vettoretti and Peltier (2018) (not shown), so that here the focus is on biogeochemistry and CO_2.

a. Configuration

The present model configuration (referred to as GLA, for glacial) features all the standard settings (i.e., the default settings one gets upon installing CESM1) of a preindustrial configuration of CESM1 (referred to herein as PRE), with the following exceptions:

In the ocean physics the Jayne (2009) prognostic representation of tidal mixing is replaced with the fixed empirical profile of Bryan and Lewis (1979), and the overflow parameterization (Danabasoglu et al. 2010) is removed altogether. The latter is done because it is not known where exactly deep water is formed during the glacial, and if and where overflows were involved. Similarly, the glacial difference in ocean bathymetry implies different tides, something that is only in the early stages of being quantified (e.g., Wilmes et al. 2019).

Ice-sheet orography and ocean bathymetry are replaced by the reconstruction of Peltier et al. (2015), and the orbital forcing parameters for the insolation are the ones from 21 000 years ago (Berger and Loutre 1991).

b. Initialization

The ocean volume resulting from the resulting 120-m sea level drop is 5.7% lower, and the concentrations of all the passive tracers [nutrients and plankton classes (see above) as well as dissolved inorganic and organic carbon (DIC and DOC, respectively)] are increased correspondingly to have the same total inventory. Salinity is increased by only 3%, 1 psu, to be in line with previous studies (e.g., Brady et al. 2013). Land cover types are the same between GLA and PRE, and wherever new land emerges as part of the sea level drop, it is covered by the type of its nearest neighbor. The initial distribution patterns (not magnitudes; see above) of all ocean tracers, including temperature and salinity, are identical in the two configurations and based on a 2000-yr-long preindustrial integration of the 1° version of CESM1 (Lindsay et al. 2014). In the land model the plant functional types are fixed; a forest grid cell will always contain only forest. This forest, however, can contain a smaller or larger leaf area depending on the growth conditions for forest (e.g., light, moisture, temperature), thereby affecting carbon content, albedo, and air–land fluxes. The initial carbon content of the land model in PRE is the result of a spinup with a preindustrial atmosphere reanalysis (Lawrence et al. 2011), whereas in GLA the initial carbon content of the land model is zero, so that it can find its own equilibrium carbon content.

c. Spinup procedure

GLA is integrated for 7000 years, in the first 3000 of which the ocean mean temperature drops from its initial preindustrial value of 3.6°–0.8°C, in agreement with the reconstructed difference from ice core noble gas records of 2.6° ± 0.2°C (Bereiter et al. 2018). The following 4000 years the temperature drift is 0.1°C, much smaller than the stadial to interstadial decrease of 0.4°C (not shown). Similarly, the final 4000 years have CO_2 drift of 1 ppm, whereas the peak-to-trough amplitude is 5 ppm and the mean concentration is 217 ppm. Thus, after year 3000 we consider the model spun up for the present purposes. PRE is integrated for 5000 years, and as for GLA we consider the model spun up after 3000 years. The only purpose of including PRE here is to understand the differences in the model carbon pools between the LGM and preindustrial times.

d. Carbon pools

A meaningful numerical experiment requires the numerical representation of the laws of nature, boundary conditions, forcing, and initial conditions. We are confident about our choices of the first three: CESM1 is a well-tested ESM and much is known about orbital forcing, orography, and bathymetry during the LGM. However, only little is known about the carbon pools. In fact, it is one of the central challenges in climate research to explain the deglacial 50% increase in CO_2 (e.g., Sigman et al. 2010). Thus, one would have to solve that problem before one could properly initialize GLA. For most tracers we chose the simple assumption of mass conservation (see above). For carbon we cannot do this, because we know that LGM CO_2 is much lower than during the preindustrial, so the various carbon pools must have been different between the preindustrial and the LGM. The only way to control CO_2

without changing the model configuration is to control the total amount of carbon in the system. We find that using 1480 PgC (1 PgC is 1 petagram or 10^{12} kg of carbon) less carbon in GLA than in PRE leads to a climate that resembles the LGM (see section 3). This number has not been the result of numerous trials and errors; it just happens to be the initial carbon content of the terrestrial biosphere in PRE. Thus, initializing GLA with zero terrestrial carbon serendipitously leads to a climate that resembles the LGM. This, together with the initial carbon content for ocean and atmosphere (the same for PRE and GLA), leads to the implicit assumption that during the glacial the inert carbon pools (ocean sediments, permafrost, or peat, none of which are part of CESM) contain 1480 PgC more than during 1850 CE (i.e., the total active carbon content in GLA is 1480 PgC lower than in PRE; see Table 1).

The size of the atmospheric carbon pool, of course, is well constrained, but no observational estimates exist for the LGM ocean [but see Galbraith and Skinner (2020) for a recent review of the vast literature]. The active land contains 580 PgC more in PRE than in GLA, which is consistent with the upper bound of the observed 330 ± 400 PgC (Ciais et al. 2012). The postulated size of the inert carbon pool, too, is consistent with observations, but barely: estimates of organic carbon burial in ocean sediment and inert-land carbon pools suggest that compared to present day, the glacial pools contained 200–500 PgC (Cartapanis et al. 2016) and 400–1000 PgC (Ciais et al. 2012) more carbon, respectively.

Last, the impact of the implied ocean sediment pools (i.e., carbonate burial) on marine biogeochemistry needs to be considered. Because CESM1 has a fixed lysocline depth, carbonate burial does not vary in response to changes in ocean chemistry. Here we attempt to constrain this effect. It is important to recognize that although the ocean in GLA contains less carbon than in PRE, the concentrations of dissolved inorganic carbon (DIC; the sum of the carbonate species) and alkalinity in GLA are greater than in PRE. This is because the decrease in the size of the ocean carbon pool during LGM is not large enough to counter the concentrating effect of decreased ocean volume. The increases in DIC and alkalinity produce a higher carbonate ion concentration in GLA than in PRE. According to the carbonate compensation concept (e.g., Archer et al. 2000), assuming a constant input of alkalinity from rivers, this increase in carbonate ion concentration would lead to increased burial of calcium carbonate, and associated removal of alkalinity and DIC in a 2:1 ratio until the original PRE carbonate ion concentration is reached. Following Tyrrell et al. (2007), we estimate that this results in a CO_2 approximately 30 ppm larger than in GLA. Thus, the carbon pools in GLA are inconsistent with observations, despite their large uncertainties [see Jeltsch-Thömmes et al. (2019) for their careful quantification], and the GLA ocean contains less carbon than it should. For the remainder of this study it is therefore assumed that the presented results are not dependent on the total carbon content of the ocean. This point will be taken up again later in the discussion.

e. Hosing and iron

It will become clear in the following section that the unforced stadials in GLA are of realistic but short duration. Furthermore,

TABLE 1. Carbon pool sizes.

Carbon pools				
Carbon (PgC)	Ocean	Atmosphere	Active land	Inert pool
LGM	35 640	460	740	1480
PRE	36 430	570	1320	—

they exhibit only minor changes in Southern Ocean carbon fluxes despite observational evidence to the contrary (see the introduction). Thus, in addition to the main simulation GLA, two more simulations are performed to investigate the importance of 1) stadial duration and 2) dust deposition. The latter is motivated by the hypothesis that in the Southern Hemisphere the warming associated with stadials leads to a moister and less dusty atmosphere, which can affect marine productivity in iron limited regions, and hence CO_2 (Martin 1990; Martínez-García et al. 2014). The extra simulation areas are as follows:

1) HOSE is branched off in the middle of the first GLA stadial (yr 4200) and submitted to an 800-yr, 0.05-Sv (1 Sv $\equiv 10^6$ m^3 s^{-1}) pulse of freshwater spread over the North Atlantic between 50° and 70°N. This pulse corresponds to an equivalent sea level rise of 1.8 m and mimics a Heinrich (1988) event.

2) IRON is identical to HOSE, but the aeolian flux of dust, which is identical in PRE, GLA, and HOSE, is everywhere reduced by 50%. Note that, unlike PRE, GLA, and HOSE, this is not an attempt to quantify the global importance of a particular process. For that there are still too many uncertainties surrounding the impact of iron on marine biogeochemistry (e.g., Tagliabue et al. 2017) and the magnitude and spatial distribution of its sources (e.g., Muglia et al. 2017). Instead, IRON is a mere sensitivity experiment. It is designed to elaborate how the observed strong stadial biogeochemical signal in the SO that is absent in GLA (see section 3) can be accounted for.

3. Results

There are three parts to this section: a basic description of model behavior, an integration of carbon fluxes by region, and a repeat of the latter for HOSE and IRON.

a. Basic description of GLA

The first stadial begins at year 3920, the first interstadial at year 4380 (the black lines in Fig. 2a, defined as the times where the Greenland temperature anomaly becomes negative or positive, respectively), the Antarctic warming ends at approximately year 4460, and CO_2 starts to decrease approximately 200 years after that. The 80-yr time lag between the onset of the interstadial and the Antarctic temperature maximum is close to the 100 years recently inferred from matching volcanic signatures in ice cores from Antarctica and Greenland (Svensson et al. 2020), but less than half of earlier methane-based estimates (Buizert et al. 2015b). The simulated stadial-to-interstadial (minimum to maximum) differences in Greenland and Antarctic temperature and
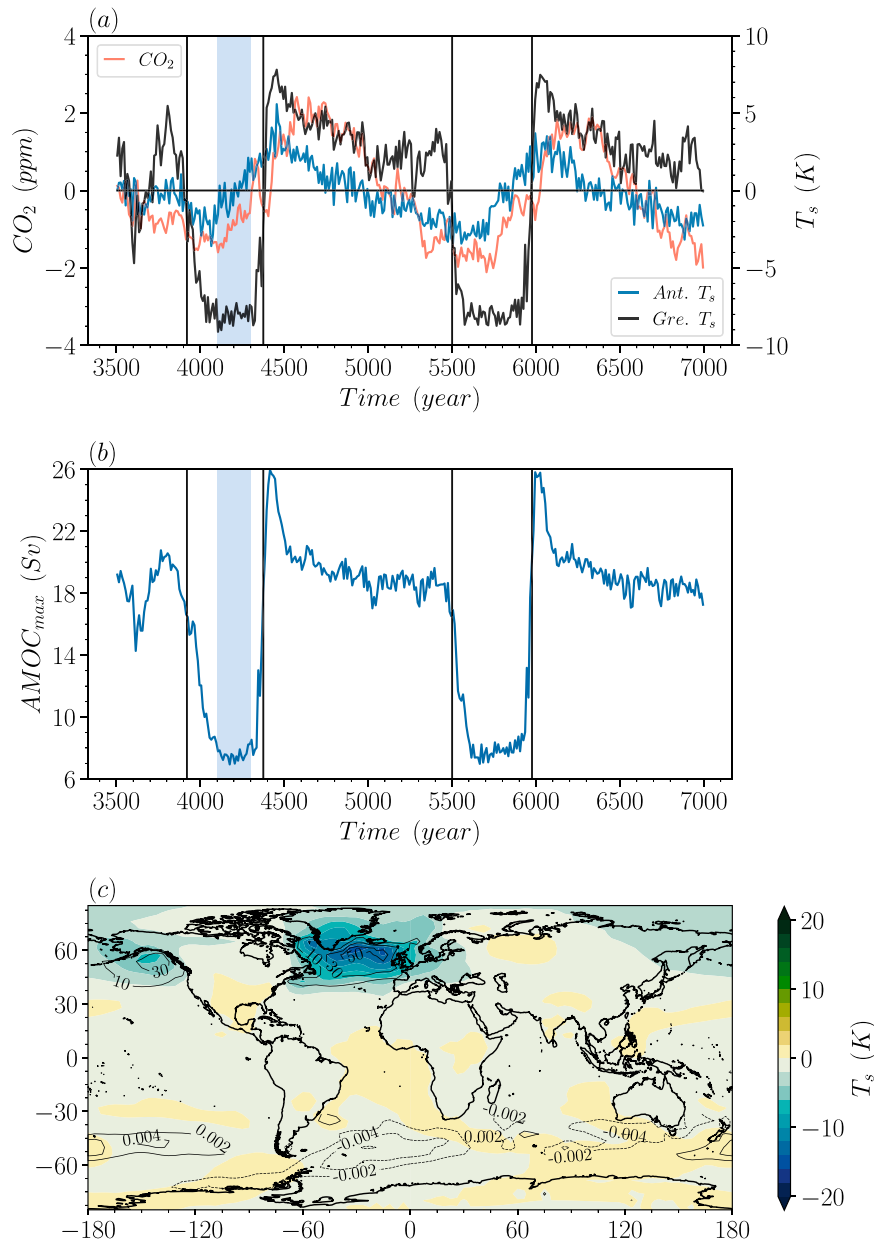
Fig. 2. (a) Greenland (50°–30°W, 65°–75°N; black) and Antarctic (multiplied by 5; blue) temperature anomalies, and CO_2 (red) anomalies (all results here are for GLA). (b) Subthermocline AMOC maximum. (c) Stadial anomalies of surface air temperature (color), Northern Hemisphere sea ice concentration (black contour, upper half of panel; %), and Southern Hemisphere wind stress (N m^{-2}).

atmospheric CO_2 are 15°C, 1.5°C, and 4 ppm, respectively. This corresponds to a 0.3°C century^{-1} Antarctic temperature rise and a 0.9 ppm century^{-1} CO_2 rise, both being slightly above the observational range of 0.6 ± 0.25 ppm century^{-1} and 0.12° ± 0.04°C century^{-1} [Zheng et al. (2021) and EPICA Community Members (2006), respectively].

As described in detail by Vettoretti and Peltier (2018), the stadial build-up of subsurface heat in the North Atlantic gives rise to a sudden emergence of polynyas in the Irminger Basin. The

resulting destruction of the vertical salinity gradient restarts the AMOC (Fig. 2b), warms the northern polar latitudes (Fig. 2c), and shifts precipitation patterns across the planet (Fig. 3a). The subtropical build-up of salinity during the stadials leads to positive density anomalies resulting in an overshoot of AMOC strength (Fig. 2b). Such an overshoot following an AMOC recovery has already been proposed by Barker et al. (2010) based on radiocarbon observations and carbonate preservation indicators in the South Atlantic. Of interest here is
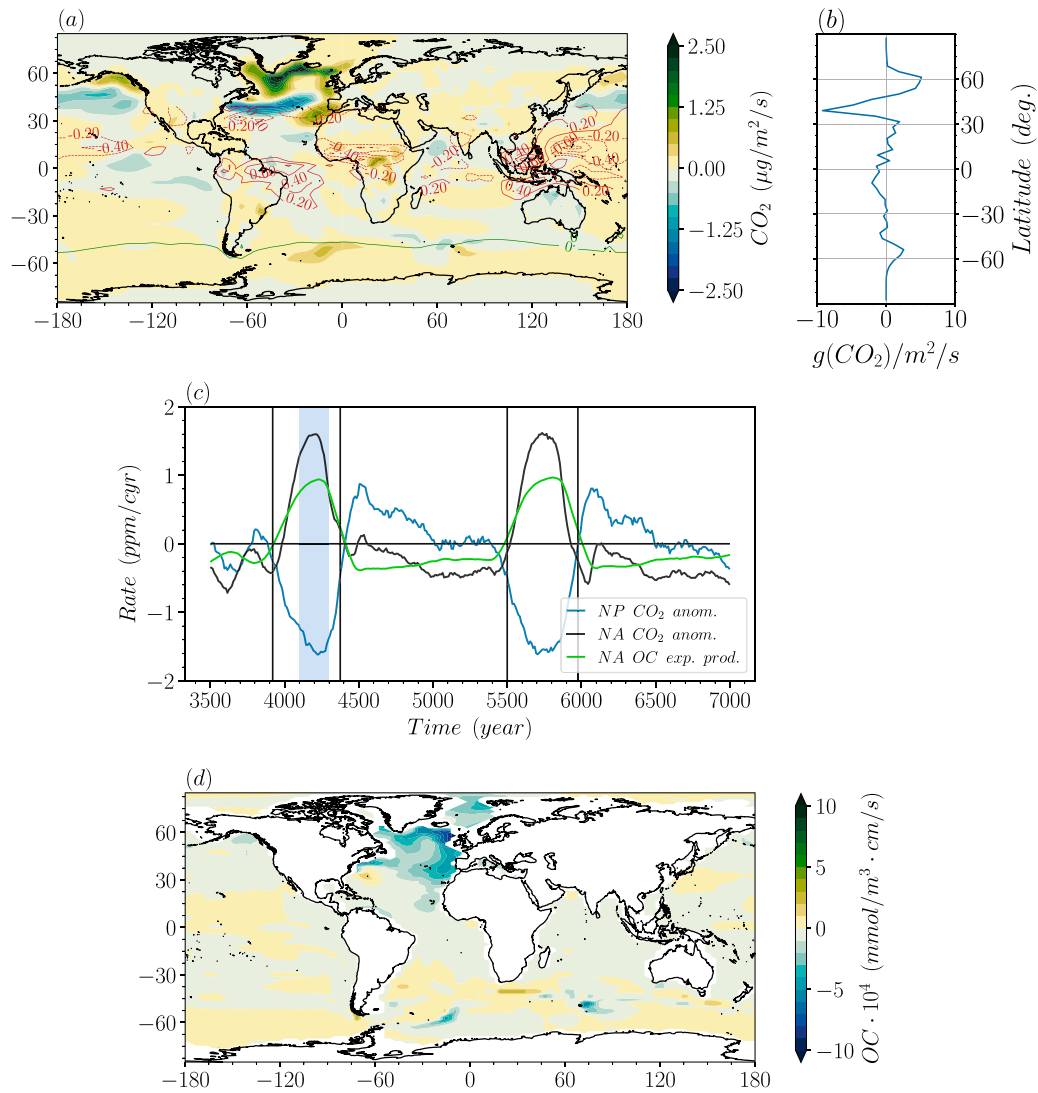
FIG. 3. (a) Stadial anomalies of air–sea/land flux of carbon (color) and tropical precipitation (red; mm day^{-1}), as well as the line of zero wind stress curl in the SO (green), which separates upwelling and downwelling regions. Negative carbon-flux anomalies indicate areas that contribute to a reduction in CO_2, which can be the result of reduced outgassing (e.g., tropical east Pacific) or increased uptake (e.g., subtropical North Atlantic). (b) Zonal integral of stadial rate anomalies. (c) Stadial anomalies of NA (black), NP (blue) CO_2, and NA export production across 700 m (green). Here, export production is converted to the equivalent rate of atmospheric CO_2 change, so lower export production will result in a positive sign. (d) Stadial anomalies of export production across 700 m (μmol C m^{-2} s^{-1}).

which of these changes affect CO_2. For the present analysis we will focus on the first stadial, and compute the anomalies as the averages of years 4100–4300 minus the averages of years 3500–6500. Other choices can reasonably be made, but will not change the overall conclusions. The main focus is on the air–sea fluxes; the impact of an AMOC collapse on the terrestrial carbon pools has been discussed already by Nielsen et al. (2019) for a preindustrial setup of the present model version: a shift of the ITCZ during stadials leads to drying of tropical rain forests and carbon release (Fig. 3a).

There are various factors that affect the air–sea fluxes of carbon: sea surface temperature and salinity, through

solubility; sea ice concentration, by isolating areas of CO_2 uptake or outgassing from the atmosphere; and wind speed, by influencing the rate of air–sea gas exchange. Then there are indirect effects like wind stress curl, by determining up- and downwelling of nutrients, and CO_2 removal by plankton through photosynthesis and subsequent dying and sinking to the abyssal oceans [the list above is not exhaustive; see Williams and Follows (2011) for a review]. Inspection of the stadial carbon flux anomalies show that the largest changes are indeed associated with North Atlantic (NA) and North Pacific (NP) cooling and associated changes in sea ice cover (cf. Figs. 2c and 3a).

b. Grouping by climate regime

The stadial flux anomalies are quite patchy, but one can meaningfully group them together into the NA or NP (both north of 30°N), the tropics (30°S–30°N), and the Southern Ocean (SO; south of 30°S), each one of which has its own particular response to the stadial onset. The flux anomalies are integrated over the respective areas and converted to rates of ppm CO_2 change per century (1 ppm CO_2 is equivalent to 2.12 PgC). This makes it easier to put the results into the context of the observed stadial CO_2 increase of 0.6 ± 0.25 ppm per century. Interestingly, the NA and NP have compensating responses to the AMOC collapse (Fig. 3b): the direct cooling leads to increased solubility in the NP, and increased uptake of carbon (Fig. 3a). While some of this is at play in the NA as well, this is more than compensated by the barrier effect of more sea ice (cf. the sea ice changes in the NP and NA) and the collapse of marine productivity (Fig. 3c).

As seen in other studies as well, this reduced efficiency of the biological pump is due to the AMOC collapse. In particular in the NA the stadial mixed layer stays shallow due to the absence of deep convection, and nutrients are trapped below the euphotic zone (e.g., Schmittner 2005). Because the present CESM version does not carry isotopes like ^{13}C, it is not possible to quantify exactly how much this reduced biological productivity contributes to the total change in NA air–sea fluxes [see Khatiwala et al. (2019) or Gu et al. (2020) for challenges and solutions to quantify the strength of the biological pump, and Shao et al. (2021) for the interpretation of ^{13}C records]. However, computing the rate anomaly of particulate organic carbon (a proxy for the strength of the biological pump) below the realm of the wind-driven circulation at 700 m suggests that much of the NA CO_2-rate anomaly may indeed be due to lower export production (Fig. 3b).

In the SO four processes modulate the air–sea fluxes of carbon: export production, midlatitude subduction (north of the zero-curl line in Fig. 3a) and upwelling (south of it), and polar deep convection (Gruber et al. 2009). Here, because of the extensive glacial sea ice cover, there is little uptake of carbon off the Antarctic coast (not shown), and hence only a negligible stadial anomaly. There are, however, changes to air–sea fluxes and the export production (Fig. 3c) between 60° and 40°S, and they are correlated with a smaller than 5% reduction in wind stress (Fig. 2c, the SO mean wind stress is on the order of 0.1–0.2 N m^{-2}). For the most part the flux anomalies are of opposite sign and lie on opposite sides of the zero-line of the mean wind stress curl (Fig. 2d), which results in a small net contribution to CO_2 (Fig. 3b). The SO CO_2 rate anomaly does, with a lag, track the SO SST anomaly (Fig. 3c), which in turn looks similar to the Antarctic temperature anomaly (Figs. 2a, 3c). As shown by Pedro et al. (2018), the stadial warming of the SO and Antarctica happens on the slow ocean time scale as seen here as well. The atmosphere, however, responds rapidly to the ITCZ shift induced by the AMOC collapse [see also Chiang and Bitz (2005) and Markle et al. (2017)]. This suggests that the immediate SO carbon release at the onset of the stadial is caused by the rapid changes to the southerly winds, whereas the later increase is caused by the slow warming of the SO. In the tropics the stadial reorganization and general weakening of the hydrological cycle (Fig. 3a) lead to reduced upwelling and outgassing in all three basins. Locally these changes are only of small amplitude (less than 5%) but add up to a sizable net contribution, opposing the SO contribution (Fig. 4a).

The analysis so far suggests that there are four ocean regions that have a stadial CO_2 rate response of similar magnitude. We propose to reduce the complexity of the problem by combining these four into two: an AMOC-forced NH response (North Atlantic and Pacific, because they show similar temperature and sea ice patterns; Fig. 2c) and a remotely wind-forced response (SO and tropics). This is not only physically meaningful, but also increases the robustness of the results because it combines different offsetting responses and uncertainties: solubility versus sea ice and export production in the former regions, and upwelling and downwelling in the latter. Furthermore, most of the water that upwells in the tropics originates in the southern midlatitudes (Pedlosky 1987) so that reduced uptake of carbon in the SO will lead to reduced outgassing in the tropics even without changes to the winds there.

Thus, we propose to explain the evolution of CO_2 as the sum of three processes, all ultimately triggered by a collapse of the AMOC. First, cooling and shifting precipitation leads to reduced terrestrial productivity and carbon loss, mainly in Africa (Fig. 3a; green line in Fig. 4b). This terrestrial carbon loss is compensated by reduced outgassing of the remote wind-forced response (the net result of reduced SO uptake and reduced tropical outgassing; red line in Fig. 4b). Changes in the NP and NA largely compensate each other so that throughout the stadials the northern mid- to high-latitude oceans play a minor role for CO_2. Second, as the SO SST continues to rise, the SO becomes an ever larger source of CO_2 (Fig. 4a), which explains the approximately 200-yr delay in the onset of the CO_2 rise during the stadial. Third, while during the stadial the northern mid- and high-latitude ocean acts as a sink of carbon, the strong rebound of NH temperature at the onset of the interstadial leads to reversal (Fig. 3b), so that the North Atlantic and Pacific, like the tropics (Fig. 4a), lead to the CO_2 rise in the first several centuries of the interstadial (black line in Fig. 4b).

It should be kept in mind that Fig. 4b illustrates the integrated anomalies with respect to year 4000, after the onset of the first stadial. Thus, the accumulated anomalies of the second stadial contain not only the results of the processes discussed above, but also long-term trends, and the effects of differences between the first and the second stadial. Two realizations provide not enough data to determine how large the variance of the stadial flux anomalies is, but Figs. 3b and 4a suggest the following: the North Atlantic and Pacific anomalies are fairly similar between the two stadials, whereas SO seems to exhibit a long-term trend, and the tropics show large interstadial variability (e.g., the red line at year 4800 in Fig. 4a). While these differences between model stadial 1 and 2 are noticeable, they are not so large to suggest that carbon flux balances are fundamentally different between different stadials. Instead, the CO_2 anomalies in Fig. 2a suggest that while there may be regional differences between various stadials they are mostly compensating.

c. Additional effects in HOSE and IRON

The multitude of similarly important but opposing regions and processes makes one wonder about the robustness of the results,
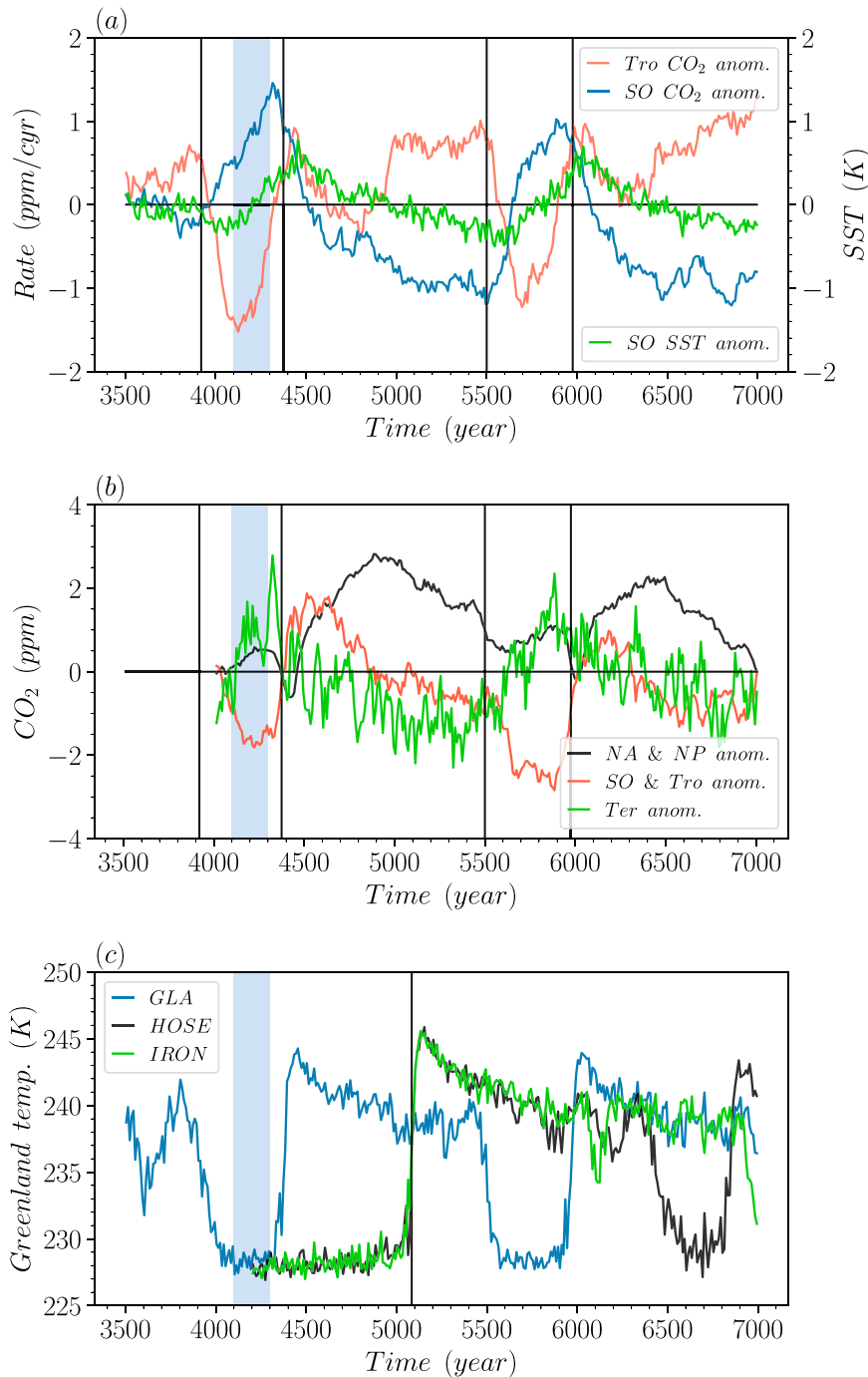
FIG. 4. (a) Stadial anomalies of tropical (30°S–30°N; red), SO (south of 30°S; blue) CO_2 rates and averaged SO SST (multiplied by 3; green). (b) Cumulative stadial CO_2 rate anomalies (with respect to year 4000) of the directly AMOC forced processes (NA and NP; black), the indirectly wind-driven component (SO and tropics; red; see text) and from land (green). (c) Stadial anomalies of Greenland temperature for GLA (blue), HOSE (black), and IRON (green).

especially since the total simulated CO_2 variability of 3–4 ppm is at the low end of the observed range. Since the stadial rate of CO_2 increase appears to be rather constant across the various stadials (Zheng et al. 2021), we decided to prolong the

simulated first GLA stadial with an 800-yr freshwater pulse (called HOSE; Fig. 4c). As in the observations, here, too, the rate of stadial CO_2 increase remains the same (Fig. 5a), and the total CO_2 increase is simply determined by the length of the stadials.
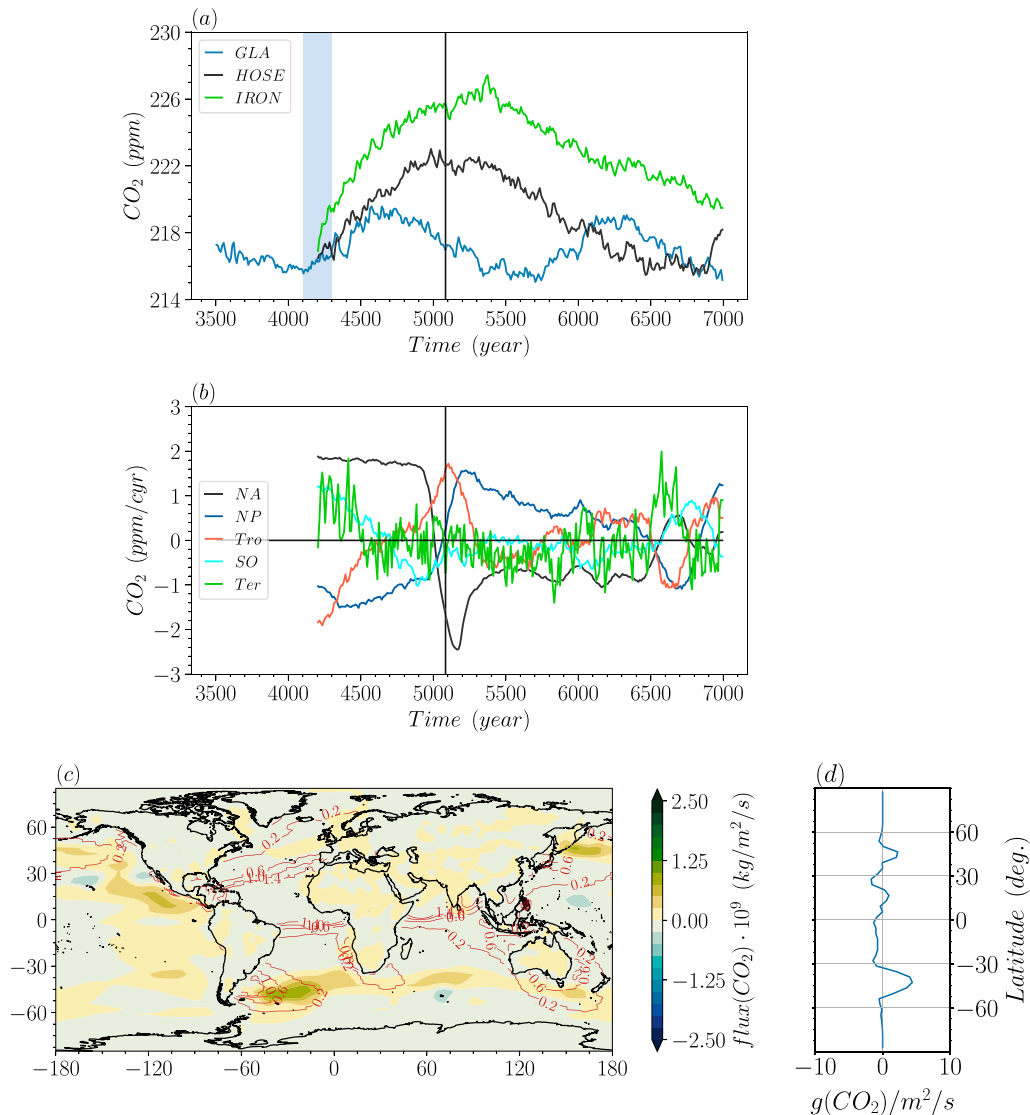
FIG. 5. (a) Stadial anomalies of CO_2 for GLA (blue), HOSE (black), and IRON (green). The vertical black line indicates the beginning of the interstadial in HOSE. (b) Stadial CO_2 rate anomalies of NA (black), NP (blue), tropics (red), SO (light blue), and terrestrial (green). (c) Differences between the stadial carbon flux anomalies of HOSE and IRON, and aeolian iron flux in HOSE. (d) Zonal integral of the differences between the stadial flux anomalies of HOSE and IRON.

Note that in contrast to standard hosing experiments where the AMOC is reduced with hosing, Greenland does not cool further here because the AMOC is already switched off. This is an indication that, at least in the model, Heinrich stadials are not fundamentally different from regular stadials; they are just longer. Similarly, a look at the CO_2 rate anomalies shows that initially the stadial anomalies are similar in GLA and HOSE, but that as the stadial wears on, the terrestrial vegetation and the upper ocean (the tropics, SO, and North Pacific) slowly come into equilibrium with respect to their carbon content [as already suggested by Siegenthaler and Wenk (1984) and Sarmiento and Toggweiler (1984)], and the CO_2 is controlled by the continued reduced carbon uptake of the North Atlantic (Fig. 5b, black curve).

Last, reducing the dust fluxes in HOSE by 50% (simulation IRON) further increases the CO_2 signal (Fig. 5a), mostly due to a reduced productivity and carbon uptake in the SO (Figs. 5c,d), in line with the conclusions of Martínez-García et al. (2014). However, the impact of this reduced uptake weakens over time, just as the other upper ocean processes in HOSE (not shown, but evidenced by the flattening of the IRON CO_2 curve in Fig. 5a).

4. Discussion

We quantified the impact of stadials on CO_2 fluxes, and the impact of changed freshwater and iron fluxes during stadials.

Of these analyses we consider the latter as the least robust; it is more a starting point for a more detailed study. During the LGM dust fluxes are considered to be several times higher than today (Rea 1994), whereas GLA uses present-day fluxes, which may lead to different sensitivities. Furthermore, in IRON dust fluxes were reduced globally, whereas the structure of the bipolar seesaw leads to an increase in the Northern Hemisphere, or at least over Greenland (NGRIP members 2004). Thus, any SO dust-flux induced CO_2 signal may be compensated by increased productivity in the North Pacific low-iron regions—although there is no observational evidence for this (Burgay et al. 2021). Of course, apart from the experimental design, modeling the iron cycle is bedeviled by its particular complexity, which can lead to vastly different outcomes for similar experiments [see Gottschalk et al. (2019) for a summary].

There are numerous previous numerical studies that try to quantify the impact of an AMOC collapse on CO_2, mostly done with models of intermediate complexity. Unfortunately, even the simulations with glacial boundary conditions do not even agree on the sign of the response, that is, if ocean and land are net sources or sinks of carbon following AMOC collapse [compare Schmittner and Galbraith (2008), Bouttes et al. (2012), and Menviel et al. (2008)]. These differences can be attributed to the effects of, first, freshwater hosing on stratification and therefore on air–sea carbon fluxes, and, second, insufficiently realistic representation of the models' atmosphere (Gottschalk et al. 2019). A detailed comparison of each of these models with CESM1 is beyond the scope of the present study, but it should be pointed out that what these models lack in realism, they compensate for in cost. Thus, if they are deemed realistic they can be used to identify sensitive model parameters (i.e, Menviel et al. 2014) and then test how robust the results are. It appears that Menviel et al. (2008) describe one such model: it has a similar carbon flux response during stadials as CESM1 (possibly because it has a dynamic atmosphere that allows for a shift of the ITCZ), but is inexpensive enough to allow for numerous sensitivity studies.

There are three ESM studies that we are aware of in which the carbon flux response to an AMOC collapse is quantified (Obata 2007; Bozbiyik et al. 2011; Nielsen et al. 2019). All three have comparable resolutions to the present CESM1, but all induce the AMOC collapse during a preindustrial climate, and the duration of their AMOC collapse is different in each. It is reassuring, though, that in each three of them, as in CESM1, the AMOC collapse is followed by terrestrial carbon release, increase of CO_2, and ocean uptake of carbon. With the exception of Nielsen et al. (2019) (whose model physics and biogeochemistry modules are identical to CESM1's) the spatial pattern of these changes differs from CESM1 and from each other, but all show the North Atlantic basin as the ocean basin that has the largest absolute and relative flux changes.

Fortunately, there are observational constraints for some of the presented regional stadial/interstadial differences. A weakened or collapsed AMOC during stadials was found to be linked with increased NA sea ice and reduced export production (e.g., Henry et al. 2016; Sadatzki et al. 2019; Rasmussen et al. 2003) and North Atlantic carbon release (Ezat et al. 2017). Outside

the North Atlantic comparisons between model results and proxy data are complicated by the fact at least the present model shows rather patchy differences between stadials and interstadials (e.g., Fig. 3c). Thus, the few available cores of sufficient resolution are not necessarily representative for a basin. The North Pacific is a case in point: whereas Kiefer et al. (2001) suggest for millennial time scale an antiphase relation between NA and NP SST, Praetorius and Mix (2014), Schlung et al. (2013), and Riethdorf et al. (2013) find an in-phase relation (the former two only for the deglaciation), whereas Kiefer and Kienast (2005) find mixed signals. More recently, Walczak et al. (2020) even suggested that NP ice sheet discharge is preceding Heinrich events.

For the Southern Ocean Jaccard et al. (2016) and Gottschalk et al. (2016) find that stadials are associated with increased Antarctic Bottom Water (AABW) production and ventilation in the Atlantic sector of the SO, as well as reduced biological export of carbon, which at least for Heinrich stadial 1 is associated with an increased partial pressure of CO_2 and presumably outgassing (Martínez-Botí et al. 2015; Shuttleworth et al. 2021). The former two occur here as well [not shown, but see Vettoretti et al. (2022) for the AABW responses in the present model]. As for the latter, Fig. 3c shows the stadial signal of particulate organic carbon export at 700 m depth in GLA. The model does not agree with the observed decrease at the two Atlantic sector sites at 40°S. However, reducing the aeolian iron deposition in IRON does lead to a strongly reduced carbon uptake (Fig. 5c) in the part of the South Atlantic that is fertilized by Patagonian dust. Thus, while the total contribution of dust-deposition variations is uncertain, they have the potential to explain regional variations in air–sea fluxes of carbon.

The most powerful constraint for the sources of stadial CO_2 increase probably comes from Bauska et al. (2018): They analyze the isotopic signature of the stadial CO_2 increases and find that it must be dominated by changes to the biosphere with both terrestrial as well as marine biology contributing. The present model does not account for isotopic compositions of carbon, but the terrestrial and marine organic carbon fluxes are computed and saved during the integration. Terrestrial release of carbon does indeed make a major contribution (Fig. 4b, as a response to the southward shift of the ITCZ; see above). The importance of changes to the marine biology are less clear. Air–sea carbon fluxes shown in Fig. 3a are the result of physical and biological processes, yet the organic carbon is partly remineralized and returned to the surface by turbulence and advection (Fig. 3c). The deviation of in situ oxygen from oxygen concentrations can be used to infer the contribution of biological processes to the ocean carbon inventory (e.g., Williams and Follows 2011). However, given uncertainties with regards to preformed oxygen levels (i.e., disequilibrium oxygen), in particular in regions of large sea ice cover, this approach is likely flawed (Khatiwala et al. 2019). In lieu of a better way, we show in Fig. 3c the stadial anomaly of export production (converted to rate of CO_2 change) below 700-m depth, which is below the subtropical overturning cells that would return the carbon to the surface in less than a century. Thus, while we cannot show unequivocally that the present results are consistent with Bauska et al. (2018), we find that reduced terrestrial and North Atlantic marine

biological productivity are indeed major contributors to stadial increase in atmospheric CO_2.

The individual processes described here are not well constrained by observations, and our confidence rests mainly on the realistic simulation of the ice-core temperature and carbon records, which represent the cumulative effect of several processes. Since we observe large compensating effects, small changes to individual processes may have an outsized impact on CO_2. Thus, a crucial next step is a model ensemble with modified ocean mixing parameters, typically the most uncertain aspect of ocean models (e.g., Eden et al. 2009). A separate interesting line of enquiry focuses on the system's sensitivity to changes in the deposition of dust. ESMs now provide enough granularity that direct comparisons between simulated and observed sedimentation rates can be made, and a simulated connection between dust deposition rates and export production can be tested, which will be the subject of our future work.

5. Summary

We have described the response of carbon fluxes in CESM to centennial-scale climate oscillations. In contrast to previous studies the oscillations were not forced through hosing, and the model physics and biogeochemistry are identical to the ones used for climate projections. The model reproduces the amplitude and relative timing of the observed Greenland and Antarctic temperature fluctuations, as well as the amplitude and relative timing of the CO_2 fluctuations. The fact that the temperature and CO_2 expressions of the oscillations are similar to the observations lends confidence also to the climate–carbon cycle interactions projected with this model into the future (e.g., Long et al. 2013).

We find that the CO_2 response to stadials consists of three stages: First, during the first centuries of stadials, anomalies in tropical land, the North Atlantic and Southern Ocean act to increase atmospheric CO_2, whereas the tropics and the North Pacific act to reduce it.

Second, 500 years after the onset of a stadial, the upper ocean and the terrestrial biosphere have reached a new equilibrium and only the reduced export production in the North Atlantic contributes to a further increase in CO_2.

Third, after the onset of an interstadial all ocean basins except for the North Atlantic release the CO_2 absorbed during the stadials, which explains the fact that CO_2 rises for the first several hundred years of interstadials.

One can condense this even further: a cooler and drier terrestrial vegetation during stadials loses carbon, and much of it is absorbed by the ocean. This carbon is then released during the early interstadial and returned to the land.

As discussed above, it has been shown before that the North Atlantic and terrestrial vegetation make a contribution to stadial CO_2 rise. What our simulations allowed us to do is to quantify their respective importance and relative timing. The simulations also provided a novel possible interpretation for the observed correlation between CO_2 and Antarctic temperature: rather than both being controlled by Southern Ocean processes, they are both controlled by the AMOC and much of the stadial extra CO_2 may not be of Southern Hemisphere origin. However, the simulations also suggest that the sensitivity of the Southern Ocean to iron fertilization may turn the global ocean from a stadial carbon sink to a carbon source.

The present findings may not be applicable for stadials longer than several centuries. This is not just because stadials of this length are not analyzed here, but also because carbon pools that we have categorized as inert (e.g., permafrost, ocean sediments) may well become active players on longer time scales. In this context it is worthwhile pointing out that in both HOSE and IRON the CO_2 increase tapers off before the end of the stadial (Fig. 5a). This suggests that it takes processes not represented in CESM1 to reproduce the CO_2 response of millennia-scale stadials. Finally, it is worth repeating that the quantification of the carbon pools in section 2 reveals that the GLA ocean does not contain enough carbon. Shortcomings in any or all of the various carbon pumps could be responsible (e.g., Eggleston and Galbraith 2018), but previous CESM1 literature (e.g., Long et al. 2013) and inspection of the present results suggests that the poor ventilation of the abyssal Pacific Ocean in CESM1 is a likely culprit.

REFERENCES

Ahn, J., and E. Brook, 2008: Atmospheric CO_2 and climate on millennial time scales during the last glacial period. *Science*, **322**, 83–85, https://doi.org/10.1126/science.1160832.

Anderson, H. J., J. B. Pedro, H. C. Bostock, Z. Chase, and T. L. Noble, 2021: Compiled Southern Ocean sea surface temperatures correlate with Antarctic isotope maxima. *Quat. Sci. Rev.*, **255**, 106821, https://doi.org/10.1016/j.quascirev.2021.106821.

Anderson, R. F., S. Ali, L. I. Bradtmiller, S. H. H. Nielsen, M. Q. Fleisher, B. E. Anderson, and L. H. Burckle, 2009: Wind-driven upwelling in the Southern Ocean and the deglacial rise in CO_2. *Science*, **323**, 1443–1448, https://doi.org/10.1126/science.1167441.

Archer, D., A. Winguth, D. Lea, and N. Mahowald, 2000: What caused the glacial/interglacial atmospheric pCO_2 cycles? *Rev. Geophys.*, **38**, 159–189, https://doi.org/10.1029/1999RG000066.

Barker, S., P. Diz, M. J. Vautravers, J. Pike, G. Knorr, I. R. Hall, and W. S. Broecker, 2009: Interhemispheric Atlantic seesaw response during the last deglaciation. *Nature*, **457**, 1097–1102, https://doi.org/10.1038/nature07770.

——, G. Knorr, M. J. Vautravers, P. Diz, and L. Skinner, 2010: Extreme deepening of the Atlantic overturning circulation during deglaciation. *Nat. Geosci.*, **3**, 567–571, https://doi.org/10.1038/ngeo921.

Bauska, T. K., E. J. Brook, S. A. Marcott, D. Baggenstos, S. Shackleton, J. P. Severinghaus, and V. V. Petrenko, 2018: Controls on millennial-scale atmospheric CO_2 variability during the last glacial period. *Geophys. Res. Lett.*, **45**, 7731–7740, https://doi.org/10.1029/2018GL077881.

——, S. A. Marcott, and E. J. Brook, 2021: Abrupt changes in the global carbon cycle during the last glacial period. *Nat. Geosci.*, **14**, 91–96, https://doi.org/10.1038/s41561-020-00680-2.

Bereiter, B., S. Shackleton, D. Baggenstos, K. Kawamura, and J. Severinghaus, 2018: Mean global ocean temperatures during the last glacial transition. *Nature*, **553**, 39–44, https://doi.org/10.1038/nature25152.

Berger, A., and M. F. Loutre, 1991: Insolation values for the climate of the last 10 million years. *Quat. Sci. Rev.*, **10**, 297–317, https://doi.org/10.1016/0277-3791(91)90033-Q.

Bouttes, N., D. M. Roche, and D. Paillard, 2012: Systematic study of the impact of freshwater perturbation on the glacial carbon cycle. *Climate Past*, **8**, 589–607, https://doi.org/10.5194/cp-8-589-2012.

Bozbiyik, A., M. Steinacher, F. Joos, and L. Menviel, 2011: Fingerprints of changes in the terrestrial carbon cycle in response to large reorganizations in ocean circulation. *Climate Past*, **7**, 319–338, https://doi.org/10.5194/cp-7-319-2011.

Brady, E. C., B. L. Otto-Bliesner, J. E. Kay, and N. Rosenbloom, 2013: Sensitivity to glacial forcing in the CCSM4. *J. Climate*, **26**, 1901–1925, https://doi.org/10.1175/JCLI-D-11-00416.1.

Brovkin, V., A. Ganopolski, D. Archer, and S. Rahmstorf, 2007: Lowering of glacial atmospheric CO_2 in response to changes in oceanic circulation and marine biogeochemistry. *Paleoceanogr. Paleoclimatol.*, **22**, PA4202, https://doi.org/10.1029/2006PA001380.

Bryan, K., and L. J. Lewis, 1979: A water mass model of the World Ocean. *J. Geophys. Res.*, **84**, 2503–2517, https://doi.org/10.1029/JC084iC05p02503.

Buizert, C., and Coauthors, 2015a: Precise interpolar phasing of abrupt climate change during the last ice age. *Nature*, **520**, 661–665, https://doi.org/10.1038/nature14401.

——, and Coauthors, 2015b: The WAIS Divide deep ice core WD2014 chronology—Part 1: Methane synchronization (68–31 ka BP) and the gas age–ice age difference. *Climate Past*, **11**, 153–173, https://doi.org/10.5194/cp-11-153-2015.

——, and Coauthors, 2018: Abrupt ice-age shifts in southern westerly winds and Antarctic climate forced from the north. *Nature*, **563**, 681–685, https://doi.org/10.1038/s41586-018-0727-5.

Burgay, F., A. Spolaor, J. Gabrieli, G. Cozzi, C. Turetta, P. Vallelonga, and C. Barbante, 2021: Atmospheric iron supply and marine productivity in the glacial North Pacific Ocean. *Climate Past*, **17**, 491–505, https://doi.org/10.5194/cp-17-491-2021.

Cartapanis, O., D. Bianchi, S. Jaccard, and E. D. Galbraith, 2016: Global pulses of organic carbon burial in deep-sea sediments during glacial maxima. *Nat. Commun.*, **7**, 10796, https://doi.org/10.1038/ncomms10796.

Chiang, J. C. H., and C. M. Bitz, 2005: Influence of high latitude ice cover on the marine intertropical convergence zone. *Climate Dyn.*, **25**, 477–496, https://doi.org/10.1007/s00382-005-0040-5.

Ciais, P., and Coauthors, 2012: Large inert carbon pool in the terrestrial biosphere during the Last Glacial Maximum. *Nat. Geosci.*, **5**, 74–79, https://doi.org/10.1038/ngeo1324.

Corrick, E. C., and Coauthors, 2020: Synchronous timing of abrupt climate changes during the last glacial period. *Science*, **369**, 963–969, https://doi.org/10.1126/science.aay5538.

Danabasoglu, G., W. G. Large, and B. P. Briegleb, 2010: Climate impacts of parameterized Nordic Sea overflows. *J. Geophys. Res. Oceans*, **115**, C11005, https://doi.org/10.1029/2010JC006243.

Dansgaard, W., and Coauthors, 1993: Evidence of general instability of climate from a 250-kyr ice-core record. *Nature*, **364**, 218–220, https://doi.org/10.1038/364218a0.

Eden, C., M. Jochum, and G. Danabasoglu, 2009: Effects of different closures for thickness diffusivity. *Ocean Modell.*, **26**, 47–59, https://doi.org/10.1016/j.ocemod.2008.08.004.

Eggleston, S., and E. D. Galbraith, 2018: The devil's in the disequilibrium: Multi-component analysis of dissolved carbon and oxygen changes under a broad range of forcings in a general circulation model. *Biogeosciences*, **15**, 3761–3777, https://doi.org/10.5194/bg-15-3761-2018.

EPICA Community Members, 2006: One-to-one coupling of glacial climate variability in Greenland and Antarctica. *Nature*, **444**, 195–198, https://doi.org/10.1038/nature05301.

Ezat, M., T. L. Rasmussen, B. Hönisch, J. Groeneveld, and P. DeMenocal, 2017: Episodic release of CO_2 from the high-latitude North Atlantic Ocean during the last 135 kyr. *Nat. Commun.*, **8**, 14498, https://doi.org/10.1038/ncomms14498.

Ferreira, D., J. Marshall, and P. Heimbach, 2005: Estimating eddy stresses by fitting dynamics to observations using a residual-mean ocean circulation model and its adjoint. *J. Phys. Oceanogr.*, **35**, 1891–1910, https://doi.org/10.1175/JPO2785.1.

Galbraith, E. D., and L. C. Skinner, 2020: The biological pump during the Last Glacial Maximum. *Annu. Rev. Mar. Sci.*, **12**, 559–586, https://doi.org/10.1146/annurev-marine-010419-010906.

Gent, P. R., and J. C. McWilliams, 1990: Isopycnal mixing in ocean circulation models. *J. Phys. Oceanogr.*, **20**, 150–155, https://doi.org/10.1175/1520-0485(1990)020<0150:IMIOCM>2.0.CO;2.

Gottschalk, J., L. C. Skinner, J. Lippold, H. Vogel, N. Frank, S. L. Jaccard, and C. Waelbroeck, 2016: Biological and physical controls in the Southern Ocean on past millennial-scale atmospheric CO_2 changes. *Nat. Commun*, **7**, 11539, https://doi.org/10.1038/ncomms11539.

——, and Coauthors, 2019: Mechanisms of millennial-scale atmospheric CO_2 change in numerical model simulations. *Quat. Sci. Rev.*, **220**, 30–74, https://doi.org/10.1016/j.quascirev.2019.05.013.

Gruber, N., and Coauthors, 2009: Oceanic sources, sinks and transport of atmospheric CO_2. *Global Biogeochem. Cycles*, **23**, GB1005, https://doi.org/10.1029/2008GB003349.

Gu, S., Z. Liu, D. W. Oppo, J. Lynch-Stieglitz, A. Jahn, J. Zhang, and L. Wu, 2020: Assessing the potential capability of reconstructing glacial Atlantic water masses and AMOC using multiple proxies in CESM. *Earth Planet. Sci. Lett.*, **541**, 116294, https://doi.org/10.1016/j.epsl.2020.116294.

Heinrich, H., 1988: Origin and consequences of cyclic ice rafting in the northeast Atlantic Ocean during the past 130,000 years. *Quat. Sci. Res.*, **29**, 142–152, https://doi.org/10.1016/0033-5894(88)90057-9.

Henry, L. G., J. F. McManus, W. B. Curry, N. L. Roberts, A. M. Piotrowski, and L. D. Keigwin, 2016: North Atlantic Ocean

circulation and abrupt climate change during the last glaciation. *Science*, **353**, 470–474, https://doi.org/10.1126/science.aaf5529.

Hurrell, J. W., and Coauthors, 2013: The Community Earth System Model: A framework for collaborative research. *Bull. Amer. Meteor. Soc.*, **94**, 1339–1360, https://doi.org/10.1175/BAMS-D-12-00121.1.

Jaccard, S. L., E. D. Galbraith, A. Martínez-García, and R. F. Anderson, 2016: Covariation of deep Southern Ocean oxygenation and atmospheric CO_2 through the last ice age. *Nature*, **530**, 207–210, https://doi.org/10.1038/nature16514.

Jayne, S. R., 2009: The impact of abyssal mixing parameterizations in an ocean general circulation model. *J. Phys. Oceanogr.*, **39**, 1756–1775, https://doi.org/10.1175/2009JPO4085.1.

Jeltsch-Thömmes, A., G. Battaglia, O. Cartapanis, S. L. Jaccard, and F. Joos, 2019: Low terrestrial carbon storage at the Last Glacial Maximum: Constraints from multi-proxy data. *Climate Past*, **15**, 849–879, https://doi.org/10.5194/cp-15-849-2019.

Khatiwala, S., A. Schmittner, and J. Muglia, 2019: Air–sea disequilibrium enhances ocean carbon storage during glacial periods. *Sci. Adv.*, **5**, eaaw4981, https://doi.org/10.1126/sciadv.aaw4981.

Kiefer, T. and M. Kienast, 2005: Patterns of deglacial warming in the Pacific Ocean: A review with emphasis on the time interval of Heinrich event 1. *Quat. Sci. Rev.*, **24**, 1063–1081, https://doi.org/10.1016/j.quascirev.2004.02.021.

——, M. Sarnthein, H. Erlenkeuser, P. M. Grootes, and A. P. Roberts, 2001: North Pacific response to millennial-scale changes in ocean circulation over the last 60 kyr. *Paleoceanography*, **16**, 179– 189, https://doi.org/10.1029/2000PA000545.

Kleppin, H., M. Jochum, B. Otto-Bliesner, C. Shields, and S. Yeager, 2015: Stochastic atmospheric forcing as cause for Greenland climate transitions. *J. Climate*, **28**, 7741–7763, https://doi.org/10.1175/JCLI-D-14-00728.1.

Lawrence, D. M., and Coauthors, 2011: Parameterization improvements and functional and structural advances in version 4 of the Community Land Model. *J. Adv. Model. Earth Syst.*, **3**, M03001, https://doi.org/10.1029/2011MS00045.

Li, C., D. S. Battisti, and C. M. Bitz, 2010: Can North Atlantic sea ice anomalies account for Dansgaard–Oeschger climate signals? *J. Climate*, **23**, 5457–5475, https://doi.org/10.1175/2010JCLI3409.1.

Lindsay, K., and Coauthors, 2014: Preindustrial-control and twentieth-century carbon cycle experiments with the Earth system model CESM1(BGC). *J. Climate*, **27**, 8981–9005, https://doi.org/10.1175/JCLI-D-12-00565.1.

Long, M. C., K. Lindsay, S. Peacock, J. K. Moore, and S. C. Doney, 2013: Twentieth-century oceanic carbon uptake and storage in CESM1(BGC). *J. Climate*, **26**, 6775–6800, https://doi.org/10.1175/JCLI-D-12-00184.1.

Markle, B. R., and Coauthors, 2017: Global atmospheric teleconnections during Dansgaard–Oeschger events. *Nat. Geosci.*, **10**, 36–40, https://doi.org/10.1038/ngeo2848.

Martin, J. H., 1990: Glacial–interglacial CO_2 change: The iron hypothesis. *Paleocenogr. Paleoclimatol.*, **5** (1), 1–13, https://doi.org/10.1029/PA005i001p00001.

Martínez-Botí, M. A., G. Marino, G. L. Foster, P. Ziveri, M. J. Henehan, J. W. B. Rae, P. G. Mortyn, and D. Vance, 2015: Boron isotope evidence for oceanic carbon dioxide leakage during the last deglaciation. *Nature*, **518**, 219–222, https://doi.org/10.1038/nature14155.

Martínez-García A., and Coauthors, 2014: Iron fertilization of the Subantarctic Ocean during the last ice age. *Science*, **343**, 1347–1350, https://doi.org/10.1126/science.1246848.

Menviel, L., A. Timmermann, A. Mouchet, and O. Timm, 2008: Climate and marine carbon cycle response to changes in the strength of the Southern Hemispheric westerlies. *Paleoceanogr. Paleoclimatol.*, **23**, PA4201, https://doi.org/10.1029/2008PA001604.

——, M. England, K. Meisser, A. Mouchet, and J. Yu, 2014: Atlantic–Pacific seesaw and its role in outgassing CO_2 during Heinrich events. *Paleoceanogr. Paleoclimatol.*, **29**, 58–70, https://doi.org/10.1002/2013PA002542.

——, P. Spence, and M. England, 2015: Contribution of enhanced Antarctic Bottom Water formation to Antarctic warm events and millennial-scale atmospheric CO_2 increase. *Earth Planet. Sci. Lett.*, **413**, 37–50, https://doi.org/10.1016/j.epsl.2014.12.050.

Moore, J. K., K. Lindsay, S. C. Doney, M. C. Long, and K. Misumi, 2013: Marine ecosystem dynamics and biogeochemical cycling in the Community Earth System Model [CESM1(BGC)]: Comparison of the 1990s with the 2090s under the RCP4.5 and RCP8.5 scenarios. *J. Climate*, **26**, 9291–9312, https://doi.org/10.1175/JCLI-D-12-00566.1.

Muglia, J., C. J. Somes, L. Nickelsen, and A. Schmittner, 2017: Combined effects of atmospheric and seafloor iron fluxes to the glacial ocean. *Paleoceanogr. Paleoclimatol.*, **32**, 1204–1218, https://doi.org/10.1002/2016PA003077.

Neale, R., J. Richter, and M. Jochum, 2008: The impact of convection on ENSO: From a delayed oscillator to a series of events. *J. Climate*, **21**, 5904–5924, https://doi.org/10.1175/2008JCLI2244.1.

Nielsen, S. B., M. Jochum, J. B. Pedro, C. Eden, and R. Nuterman, 2019: Two-timescale carbon cycle response to an AMOC collapse. *Paleoceanogr. Paleoclimatol.*, **34**, 511–523, https://doi.org/10.1029/2018PA003481.

NGRIP members, 2004: High-resolution record of Northern Hemisphere climate extending into the last interglacial period. *Nature*, **431**, 147–151, https://doi.org/10.1038/nature02805.

Obata, A., 2007: Climate-carbon cycle model response to freshwater discharge into the North Atlantic. *J. Climate*, **20**, 5962–5976, https://doi.org/10.1175/2007JCLI1808.1.

Pedlosky, J., 1987: An inertial theory of the equatorial undercurrent. *J. Phys. Oceanogr.*, **17**, 1978–1985, https://doi.org/10.1175/1520-0485(1987)017<1978:AITOTE>2.0.CO;2.

Pedro, J., M. Jochum, C. Buizert, F. He, S. Barker, and S. Rasmussen, 2018: Beyond the bipolar seesaw: Toward a process understanding of interhemispheric coupling. *Quat. Sci. Rev.*, **192**, 27–46, https://doi.org/10.1016/j.quascirev.2018.05.005.

Peltier, W. R., and G. Vettoretti, 2014: Dansgaard–Oeschger oscillations predicted in a comprehensive model of glacial climate: A "kicked" salt oscillator in the Atlantic. *Geophys. Res. Lett.*, **41**, 7306–7313, https://doi.org/10.1002/2014GL061413.

——, D. F. Argus, and R. Drummond, 2015: Space geodesy constrains ice-age terminal deglaciation: The global ICE-6G_C (VM5a) model. *J. Geophys. Res. Solid Earth*, **120**, 450–487, https://doi.org/10.1002/2014JB011176.

Praetorius, S. K., and A. C. Mix, 2014: Synchronization of North Pacific and Greenland climates preceded abrupt deglacial warming. *Science*, **345**, 444–448, https://doi.org/10.1126/science.1252000.

Rae, J. W. B., and Coauthors, 2018: CO_2 storage and release in the deep Southern Ocean on millennial to centennial timescales. *Nature*, **562**, 569–573, https://doi.org/10.1038/s41586-018-0614-0.

Rasmussen, T. L., and Coauthors, 2003: Millennial-scale glacial variability versus Holocene stability: Changes in planktic and benthic foraminifera faunas and ocean circulation in the North

Atlantic during the last 60000 years. *Mar. Micropaleontol.*, **47**, 143–176, https://doi.org/10.1016/S0377-8398(02)00115-9.

Rea, D. K., 1994: The paleoclimatic record provided by eolian deposition in the deep sea: The geologic history of wind. *Rev. Geophys.*, **32**, 159–195, https://doi.org/10.1029/93RG03257.

Riethdorf, J., L. Max, D. Nuernberg, and R. Tiedemann, 2013: Millennial-scale variability of marine productivity and terrigenous matter supply in the western Bering Sea over the past 180 kyr. *Climate Past Discuss.*, **8**, 6135–6198, https://doi.org/10.5194/cpd-8-6135-2012.

Sadatzki, H., and Coauthors, 2019: Sea ice variability in the southern Norwegian Sea during glacial Dansgaard–Oeschger climate cycles. *Sci. Adv.*, **5**, eaau6174, https://doi.org/10.1126/sciadv.aau6174.

Sarmiento, J. L., and J. R. Toggweiler, 1984: A new model for the role of oceans in determining atmospheric P CO_2. *Nature*, **308**, 621–624, https://doi.org/10.1038/308621a0.

Schlung, S. A., and Coauthors, 2013: Millennial-scale climate change and intermediate water circulation in the Bering Sea from 90 ka: A high-resolution record from IODP Site U1340. *Paleoceanogr. Paleoclimatol.*, **28**, 54–67, https://doi.org/10.1029/2012PA002365.

Schmittner, A., 2005: Decline of the marine ecosystem caused by a reduction in the Atlantic overturning circulation. *Nature*, **434**, 628–633, https://doi.org/10.1038/nature03476.

——, and E. D. Galbraith, 2008: Glacial greenhouse-gas fluctuations controlled by ocean circulation changes. *Nature*, **456**, 373–376, https://doi.org/10.1038/nature07531.

Scholze, M., W. Knorr, and M. Heimann, 2003: Modelling terrestrial vegetation dynamics and carbon cycling for an abrupt climatic change event. *Holocene*, **13**, 327–333, https://doi.org/10.1191/0959683603hl625rp.

Shao, J., L. D. Stott, L. Menviel, A. Ridgwell, M. Ödalen, and M. Mohtadi, 2021: The atmospheric bridge communicated the $\delta^{13}C$ decline during the last deglaciation to the global upper ocean. *Climate Past*, **17**, 1507–1521, https://doi.org/10.5194/cp-17-1507-2021.

Shields, C., D. A. Bailey, G. Danabasoglu, M. Jochum, J. T. Kiehl, S. Levis, and S. Park, 2012: The low-resolution CCSM4. *J. Climate*, **25**, 3993–4014, https://doi.org/10.1175/JCLI-D-11-00260.1.

Shuttleworth, R., and Coauthors, 2021: Early deglacial CO_2 release from the sub-Antarctic Atlantic and Pacific Oceans. *Earth Planet. Sci. Lett.*, **554**, 116649, https://doi.org/10.1016/j.epsl.2020.116649.

Siegenthaler, U., and T. Wenk, 1984: Rapid atmospheric CO_2 variations and ocean circulation. *Nature*, **308**, 624–626, https://doi.org/10.1038/308624a0.

Sigman, D. M., M. P. Hain, and G. H. Haug, 2010: The polar ocean and glacial cycles in atmospheric CO_2 concentration. *Nature*, **466**, 47–55, https://doi.org/10.1038/nature09149.

Svensson, A., and Coauthors, 2020: Bipolar volcanic synchronization of abrupt climate change in Greenland and Antarctic ice cores during the last glacial period. *Climate Past*, **16**, 1565–1580, https://doi.org/10.5194/cp-16-1565-2020.

Tagliabue, A., A. R. Bowie, P. W. Boyd, K. N. Buck, K. S. Johnson, and M. A. Saito, 2017: The integral role of iron in ocean biogeochemistry. *Nature*, **543**, 51–59, https://doi.org/10.1038/nature21058.

Tyrrell, T., S. G. Shepard, and S. Castle, 2007: The long-term legacy of fossil fuels. *Tellus*, **59B**, 664–672, https://doi.org/10.1111/j.1600-0889.2007.00290.x.

Vettoretti, G., and W. R. Peltier, 2018: Fast physics and slow physics in the nonlinear Dansgaard–Oeschger relaxation oscillation. *J. Climate*, **31**, 3423–3449, https://doi.org/10.1175/JCLI-D-17-0559.1.

——, P. Ditlivsen, M. Jochum, and S. Rasmussen, 2022: Atmospheric CO_2 control of spontaneous millennial-scale ice age climate oscillations. *Nat. Geosci.*, **15**, 300–306, https://doi.org/10.1038/s41561-022-00920-7.

Walczak, M., and Coauthors, 2020: Phasing of millennial-scale climate variability in the Pacific and Atlantic Oceans. *Science*, **370**, 716–720, https://doi.org/10.1126/science.aba7096.

Williams, R., and M. J. Follows, 2011: *Ocean Dynamics and the Marine Carbon Cycle*. Springer, 434 pp.

Wilmes, S.-B., A. Schmittner, and J. A. M. Green, 2019: Glacial ice sheet extent effects on modeled tidal mixing and the global overturning circulation. *Paleoceanogr. Paleoclimatol.*, **34**, 1437–1454, https://doi.org/10.1029/2019PA003644.

Zhang, X., G. Lohmann, G. Knorr, and C. Purcell, 2014: Abrupt glacial climate shifts controlled by ice sheet changes. *Nature*, **512**, 290–294, https://doi.org/10.1038/nature13592.

——, G. Knorr, G. Lohmann, and S. Barker, 2017: Abrupt North Atlantic circulation changes in response to gradual CO_2 forcing in a glacial climate state. *Nat. Geosci.*, **10**, 518–523, https://doi.org/10.1038/ngeo2974.

Zheng, P., J. Pedro, M. Jochum, S. Rasmussen, and Z. Lai, 2021: Different trends in Antarctic temperature and atmospheric CO_2 during the last glacial. *Geophys. Res. Lett.*, **48**, e2021GL093868, https://doi.org/10.1029/2021GL093868.